

Nao-Aki Noda^{1,*}
Hongfang Zhai¹
Kakeru Takata¹
Yoshikazu Sano¹
Yasushi Takase¹
Fei Ren²
Ryo Kawano¹
Toshihiko Umekaga¹
Yuji Yonezawa³
Hiroyuki Tanaka¹

Elucidation of flow characteristics in honeycomb structure to design nanobubble generating apparatus

Abstract

This study deals with nanobubble generator using honeycomb structures producing a large amount of water including large nanobubble density in a short time. Here, the nanobubble generating performance is investigated for large and small apparatus having different honeycomb cell dimensions by applying a computational fluid dynamics (CFD) coupled with a population balance model (PBM). The CFD simulation shows significant pressure drop and shear stress occur in the bubbly flow in the honeycomb cell. The numerical model is based on the Eulerian multiphase model and the PBM is used to calculate the bubble size distribution. The obtained CFD-PBM results are compared with the experimental results for large and small apparatus. The results show that bubble size distributions in the honeycomb structure under different inlet absolute pressure can be predicted by the PBM. It may be concluded that the maximum shear stress is the main controlling factor for the nanobubble generation.

Keywords: Nanobubble, Honeycomb, Computational Fluid Dynamics, Population Balance Method

¹Mechanical Engineering Department, Kyushu Institute of Technology, Sensui-cho 1-1 Tobata-ku Kitakyushu-shi Fukuoka 804-8550.

²School of Mechanical and Automotive Engineering, Qilu University of Technology, No.3501, Daxue Road, Changqing, Jinan, Shandong, China

³Marufukusuisan Corp., Ltd.

Kokurakita-ku Nisimoinato-cho Kitakyushu-shi Fukuoka 803-080.

* Corresponding author: Nao-Aki Noda (E-mail:noda.naoaki844@mail.kyutech.jp), Mechanical Engineering Department, Kyushu Institute of Technology, Sensui-cho 1-1 Tobata-ku Kitakyushu-shi Fukuoka 804-8550.

1 Introduction

In recent years, nanobubble technology has drawn great attention due to their wide applications in wide fields of science and technology, such as life science,

This is the peer reviewed version of the following article: <https://onlinelibrary.wiley.com/doi/full/10.1002/ceat.201900437>, which has been published in final form at <https://doi.org/10.1002/ceat.201900437>. This article may be used for non-commercial purposes in accordance with Wiley Terms and Conditions for Use of Self-Archived Versions.

machinery industry, medical engineering, chemical, agriculture, fisheries and civil engineering [5-8], especially focusing on washing several items, sterilization and promoting germination. A lot of previous studies discussed microbubble generation whose diameter $d=1-100 \mu\text{m}$ [7, 9-11]. However, no detail study is available for nanobubble or ultrafine bubble whose diameter $d \leq 0.1 \mu\text{m}$. Therefore, in this paper, nanobubble generation mechanism and generation ability will be studied in the numerical simulation and experiment.

This study mainly focuses on the honeycomb structure having excellent efficiency for nanobubble generation [11-14]. Table 1 compares nanobubble generation abilities using the honeycomb structure and Venturi tube previously reported. As shown in Table 1, although similar nanobubble densities can be obtained after 30 minutes, the honeycomb generator has more than 50 times larger flow rate compared to Venturi tube generator.

The previous visualization experiments indicated that the nitrogen bubbles in water gradually elongate and divide by going through the honeycomb cells [15-17]. The previous computational fluid dynamics (CFD) showed in the honeycomb structures the pressure decreases from the upstream to the downstream and the shear stress takes several peaks at the corners of the cells; and therefore, the pressure drop and the peak shear stress may affect nanobubble generation in a large apparatus in Fig. 1(a) [18, 19].

In this study, a small apparatus in Fig. 1(b) will be newly considered for 100 liters water tank in comparison with the large apparatus in Fig.1(a) used for 1000 liters water tank. In the honeycomb structures in Fig.1 (c) included in those apparatus, the nanobubble generating performance will be investigated experimentally by varying the cell size. The bubble size distributions under different inlet absolute pressure will be also analyzed by the CFD-PBM simulation coupled with the RNG k- ϵ turbulence model [19-21]. The final goal of this study is to design the honeycomb structures generating nanobubble efficiently with clarifying the mechanism.

Table 1. Comparison of nanobubble generation ability

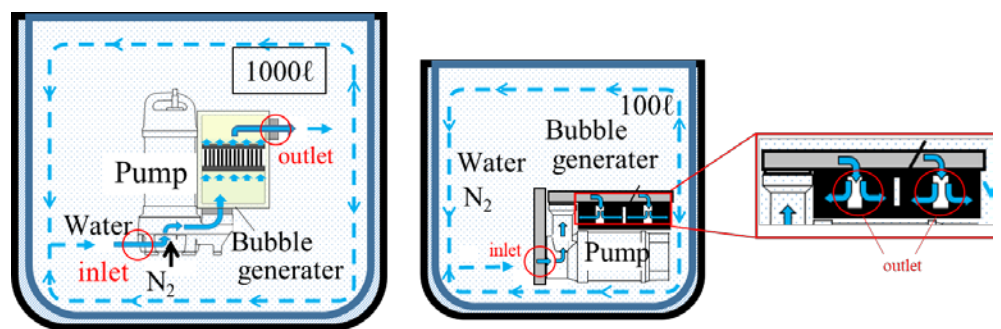
	Nanofresher using honeycomb structure by NANOX	Ultrafine GALF using Venturi tube by IDEC
Q [l/min]	550	16.7
p_a [MPa]	0.45	0.3
N_d [particle/ml] after 30 min	1.7×10^8	1.42×10^8

2 Nanobubble generators using honeycomb structures

Fig. 1(a), (b) shows the schematic illustrations of the large apparatus for 1000l tank and the small apparatus for 100l tank, both of them having parallel honeycomb units and immersed in water in the tank. The water and the nitrogen gas are pumped into those apparatus together and flow into the honeycomb units. Fig.1(c) shows a unit

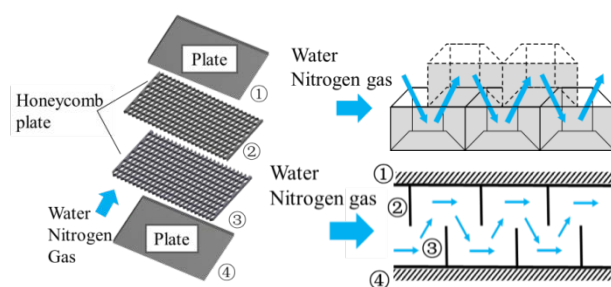
of the honeycomb structure consisting of a pair of honeycomb plates and upper and lower plates for sealing both ends. Total 16 honeycomb units are installed in the small apparatus and total 12 honeycomb units are installed in the large apparatus. In addition, Fig. 1(c) illustrates nitrogen-water mixture flow through the honeycomb structure. Between each honeycomb unit, complex flow channels are formed by the overlapped honeycomb plates, in which the honeycomb plates are shifted by 1/2 cell in the flow direction. When the nitrogen-water mixture flows through the apparatus, the bubbles become finer, and the water flowing out of the generator flows into the apparatus again. This cycle has been repeated, and miniaturization effect continues [16]. Table 2 shows the details of the small experimental apparatus in comparison with the large apparatus used in the previous study [19]. Because the small apparatus deals with 0.1 times of the water amount of the large apparatus, a low output pump is used.

The nano-particle analyser Nano Sight LM10-HS is used to measure the nanobubble number density [16, 17, 22, 23]. Tracking Brownian motion of all particles recognized on the screen and using the Stokes-Einstein equation, the particle size is obtained from the moving velocity of the particles. The nanobubble number density is measured from collected samples under stable states after 30 minutes to 1 hour from the experiment start where micro bubbles larger than 1 μ m diameter disappear.



(a) Large apparatus including parallel 12 honeycomb units

(b) Small apparatus including parallel 16 honeycomb units



(c) Illustration of a honeycomb unit.

Figure 1. (a) Large and (b) Small apparatus including parallel honeycomb unit, and (c) Illustration of a honeycomb unit.

Table 2. Details of the experimental apparatus

Item	Large apparatus	Small apparatus
Pump	Submersible pump (80TM23.7)	Submersible pump (50TMLS2.4S)
Output [kW]	3.7[kW], (60Hz)	0.4[kW], (60Hz)
Flow rate [ℓ/min]	400[ℓ/min]	270[ℓ/min]
Cell size [mm]	6.1[mm]	3.9[mm]
Cell height [mm]	10[mm]	4[mm]
Cell number*	3510	1840
Water amount [ℓ]	Tap water, 1000[ℓ]	Tap water, 100[ℓ]
Gas	Nitrogen	Nitrogen
Flow rate [ℓ/min]	5.0[ℓ/min]	1.0[ℓ/min]
Pressure [MPa]	0.30[MPa]	0.20[MPa]

*Upper cell + Lower cell

The nanobubble generation efficiency varies depending on the different target water volume, honeycomb cell size used and pump output. Therefore, between the small and large apparatus, the nanobubble number density per cell and per cycle will be compared.

Table 3 compares the experimental conditions between the large and small apparatus. Fig. 2 shows the variation of nanobubble number density for the large and small apparatus after the experiment starts. In Fig.2, the nanobubble number density of small apparatus achieves the target value after 10 minutes and increases further. Compared to large apparatus, the small apparatus can achieve this shortly.

Table 3. Experimental conditions between the large and small apparatus

Experimental conditions	Large apparatus	Small apparatus
Power P_w [kW]	3.7[kW]	0.4[kW]
Wall Thickness [mm]	0.5[mm]	1[mm]
Pressure p_a [MPa]	0.45[MPa]	0.16[MPa]
Flow rate Q [ℓ/min]	550[ℓ/min]	103[ℓ/min]

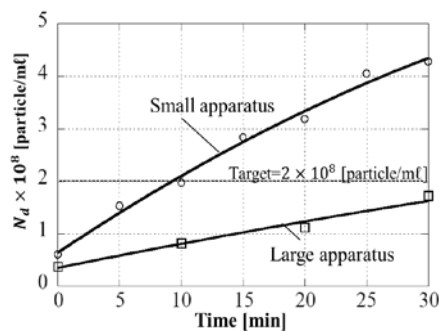


Figure 2. Nanobubbles number density variation for large and small apparatus after the experiment starts

3 Method of analysis

3.1 Computational fluid dynamics for shear stress distribution

In this study, all computations are performed using the commercial CFD software FLUENT 16.2. In this analysis, simplified honeycomb channels are used to realize the internal structure of the honeycomb-type bubble generator. Fig 3 shows a 3-row periodic model for large and small apparatuses. Since the results of 3-row periodic model is close to the results of 5-row model, in this study the 3-row periodic model is chosen. The dimensions of the honeycomb cells are shown in Table 2. At the inlet and outlet, the pressure boundary conditions are adopted. The 3-row periodic model has the periodic boundary conditions. The k- ϵ model is used to simulate the turbulent flow. The turbulent intensity T_I is expressed by Eq. (1) [24].

$$T_I \equiv \frac{U_i}{U_{avr}} = 0.16(Re)^{-\frac{1}{8}} \quad (1)$$

From Reynolds number obtained in preliminary analysis $Re = 180 \sim 200$, the turbulent intensity is calculated as $T_I = 10$. At this low range of Reynolds number, the turbulent viscosity is low and does not affect the results. Also, CFD software FLUENT16.2 uses $T_I = 10$ as the default value.

The shear stress can be calculated as the product of strain rate and viscosity. The strain tensor e_{ij} is expressed by (Eq. (2)) [25]

$$e_{ij} = \frac{1}{2} \left(\frac{\partial U_i}{\partial x_j} + \frac{\partial U_j}{\partial x_i} \right) \quad (2)$$

This tensor has three scalar invariants, one of which is called the shear strain rate I (Eq. (3)).

$$I = \left[2 \frac{\partial U_i}{\partial x_j} e_{ij} \right]^{\frac{1}{2}} \quad (3)$$

Equation (3) is expressed as Eq. (4) using velocity components U_x, U_y, U_z .

$$I = \left[2 \left\{ \left(\frac{\partial U_x}{\partial x} \right)^2 + \left(\frac{\partial U_y}{\partial y} \right)^2 + \left(\frac{\partial U_z}{\partial z} \right)^2 \right\} + \left(\frac{\partial U_x}{\partial y} + \frac{\partial U_y}{\partial x} \right)^2 + \left(\frac{\partial U_x}{\partial z} + \frac{\partial U_z}{\partial x} \right)^2 + \left(\frac{\partial U_y}{\partial z} + \frac{\partial U_z}{\partial y} \right)^2 \right]^{\frac{1}{2}} \quad (4)$$

Scalar invariants in Eq. (4) are used to express shear strain rates.

Fig.3 shows the 3-row periodic model used for large and small apparatus. For example, small apparatus includes honeycomb cell whose dimensions are 2.2mm

length and 1mm thickness. Table 4 shows the analysis conditions of the small apparatus.

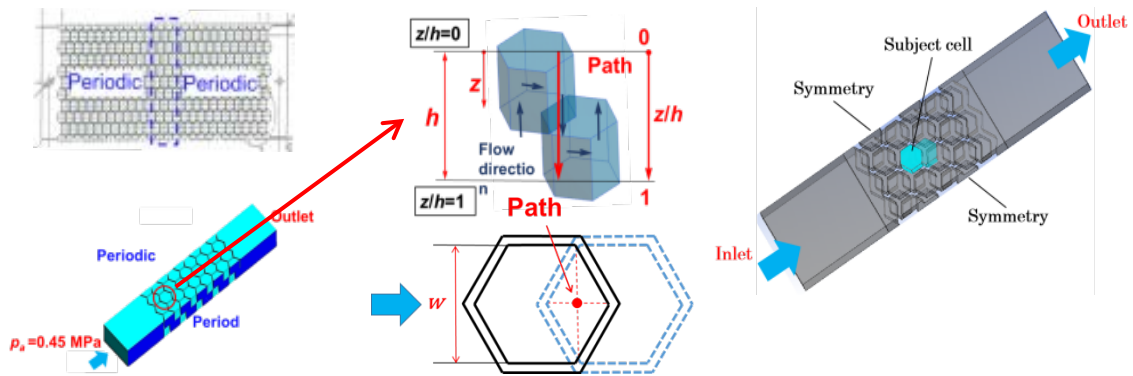


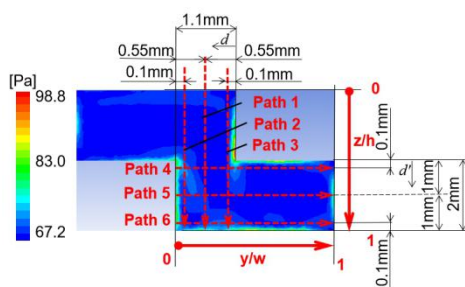
Figure 3 Periodic 3-row model used for large and small apparatus

Table 4. Analysis conditions for small apparatus

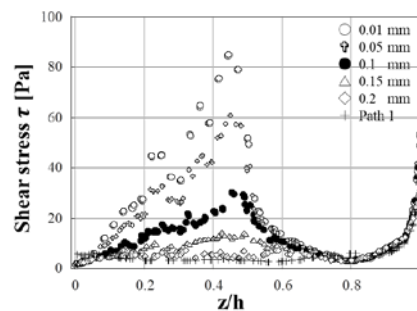
Item	Specification
Inlet absolute pressure [MPa]	0.16[MPa]
Outlet absolute pressure [MPa]	0.10[MPa]
Turbulent intensity [%]	10[%]
Turbulent viscosity ratio	10

Fig. 4 (a) shows the shear stress variation with the definition of Path1- Path 6 in the honeycomb cell of the small apparatus. As shown in Fig.4 (a), Path 1 and 5 are located along the center of the flow path, and Paths 2, 3, 4, 6 are along near the wall.

Fig. 4 (b) illustrates the shear stress variations along the vertical path z/h in Fig. 4(a) for the fixed distance from the wall $d=0.1\sim 2\text{mm}$. The horizontal axis z/h indicates the dimensionless distance from the bottom of the cell. The maximum shear stress τ_{max} appears near the corner as a peak value. As shown in Fig. 4(b), since the scatter of τ_{max} becomes larger for small distance from the wall, $x = 0.1\text{mm}$ is used to show τ_{max} in the following discussion.



(a) Shear stress variation with the definition of Path1-6



(b) Shear stress distribution along the path when the distance d from the wall is fixed

Figure 4. (a) Shear stress variation with the definition of Path1- 6, (b) Shear stress distribution along the path for fixed distance d from the wall.

3.2 Population balance method coupled with CFD focusing on bubble size distribution

The population balance method (PBM) is used to simulate the nanobubble number density distribution. A progress in the CFD simulation of bubbly flow is the coupling of the population balance model (PBM) into CFD models, namely the CFD-PBM coupled model [26, 27]. The population balance method is for tracking the size distribution of the dispersed phase and accounting for the breakage and coalescence effects in bubbly flows [20, 21]. The analysis model is shown in Fig. 3. The CFD-PBM analysis conditions of the small apparatus are shown in Table 5. The pressure boundary conditions are adopted. The number of bubble bins is classified 10 groups as shown in Table 6. Table 6 presents diameters of bubble bins tracked in this simulation. The bin 8 specifying 1280nm is chosen as the initial size at the inlet. The nano-particle analyser Nano Sight LM10-HS used in this study can detect the bubbles with the diameter in the range $x = 1-1000\text{nm}$. As shown in Table 6, the bubble bin number 1-7 are set with in this diameter range.

Table 5. CFD-PBM analysis conditions of the small apparatus

Item	Specification
Inlet absolute pressure [MPa]	0.16[MPa]
Outlet absolute pressure [MPa]	0.10[MPa]
gas volume fraction	0.00971
Initial bubble size [nm]	1280[nm]

Table 6. Diameter of each bubble bin

Bubble bin number	1	2	3	4	5	6	7	8	9	10
Mean bubble diameter [nm]	10	20	40	80	160	320	640	1280	2560	5210

The Euler-Euler two-fluid model is used in the CFD-PBM approach [28, 29] coupled with the RNG k- ϵ turbulence model. For the bubbly flow in the honeycomb structure, the liquid is treated as a continuous primary phase and the gas as a dispersed secondary phase.

The population balance equation is written in terms of volume fraction of bubble size i ,

$$\frac{\partial(\rho_p \alpha_i)}{\partial t} + \nabla \cdot (\rho_p \vec{u}_i \alpha_i) = \rho_p V_i (B_{ag,i} - D_{ag,i} + B_{br,i} - D_{br,i}) \quad (5)$$

where α_i is the volume fraction of the bubble size i and it is defined as

$$\alpha_i = N_i V_i \quad i=0,1,\dots,N-1 \quad (6)$$

where V_i is the volume of the bubble size i and N_i is defined as

$$N_i(t) = \int_{V_i}^{V_{i+1}} n(V,t) dV. \quad (7)$$

The B_{ag} is called birth rate of bubbles due to aggregation, given by

$$B_{ag} = \frac{1}{2} \int_0^V \Omega_{ag}(V-V',V) n(V-V',t) n(V',t) dV' \quad (8)$$

and the D_{ag} is called death rate of bubbles due to aggregation, given by

$$D_{ag} = \int_0^\infty \Omega_{ag}(V,V') n(V,t) n(V',t) dV'. \quad (9)$$

The birth rate of bubbles due to breakage B_{br} is given by (10) and the death rate of due to breakage D_{br} is given by (11)

$$B_{br} = \int_{\Omega_V} \lambda g(V) \beta(V|V') n(V',t) dV' \quad (10)$$

$$D_{br} = g(V) n(V,t). \quad (11)$$

The breakage formulation for the discrete method in this work is based on the Hagesather method [30]. It is assumed that there is no breakage for the smallest bubble class.

4. Results of CFD analysis

4.1 Absolute pressure and shear stress distribution

Fig.5 shows the absolute pressure Pa and the shear stress τ along the Paths 1-3 in Fig.4. Fig.5 (a), (b), (c) shows the results in the longitudinal paths and Fig.5 (d), (e), (f) shows the results in the lateral paths. The horizontal axis in Fig.5 shows the dimensionless coordinates z/h and y/w . The vertical axis in Fig.5 shows pressure Pa and shear stress τ along the flow path. Along the longitudinal Paths 1, 2, 3 in Fig 4, with increasing z/h , the pressure decreases initially and finally increases. The total pressure drop is about 0.01 along Paths 1, 2, 3.

The maximum shear stress appears as $\tau = 30\text{Pa}$ at $z/h = 0.5$ along the longitudinal Paths 2, 3. The maximum shear stress appears near the cell corner. The pressure drop and the shear stress in the longitudinal paths in Fig.5 (a), (b), (c) are larger than the pressure drop and the shear stress in lateral paths in Fig.5 (d), (e), (f).

From Fig.5, the absolute pressure decreases initially and finally increases along the Paths, and the shear stress has a high value near the corner close to the wall, and many nanobubbles can be generated near the corner. Therefore, Path 3 is focused

since Path 3 includes the maximum shear stress to compare the performance of large apparatus and small apparatus.

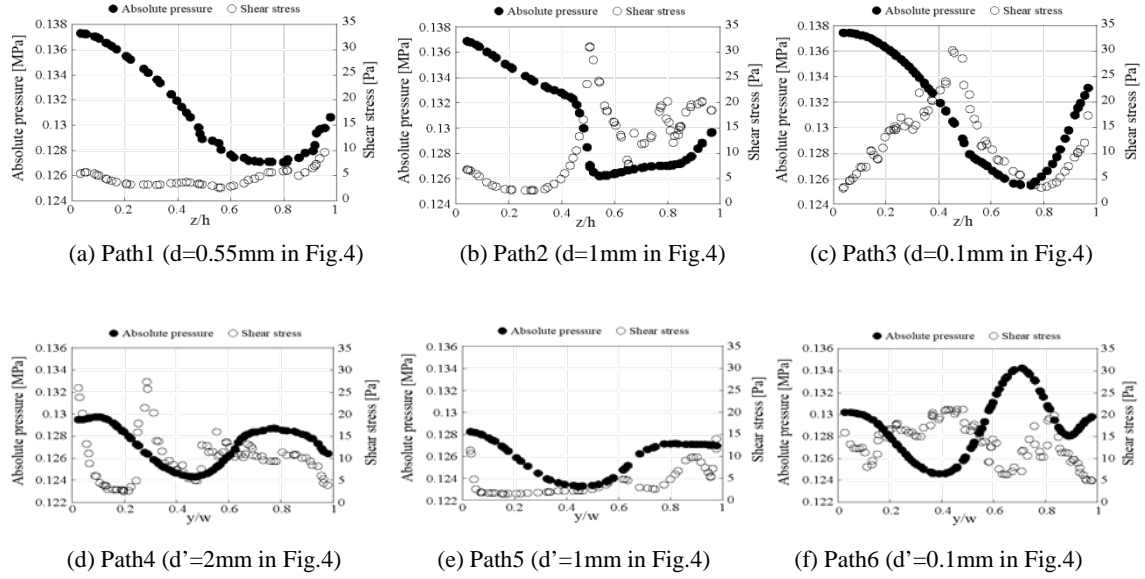


Figure 5. Absolute pressure and shear stress distribution and path (a)(b)(c) is longitudinal, path (d)(e)(f) is lateral in **Fig.4**

4.2 Comparison between the experiment and CFD results

From the experiment and fluid analysis results, the performance of large and small apparatus are compared. Table 7 shows experimental results of large apparatus in Fig. 1(a) and small apparatus in Fig. 1(b). Since the pump output, water amount and honeycomb cell dimensions are different as shown in Table 7, the nanobubble number density per cell and per cycle are compared between the large and small apparatus. The nanobubble number density per cell per cycle after 30 minutes ρ_d^{exp} is calculated from the nanobubble number density N_d^{exp} , the number of cycles of water amount N_{cycle} defined in Eq. (12) and the total number of cells N_{cell} are shown in Eq. (13).

$$N_{cycle} = (Q \cdot t) / V \quad (12)$$

$$\rho_d^{exp} = N_d^{exp} / (N_{cell} \cdot N_{cycle}) \quad (13)$$

As shown in Table 7, the nanobubble number density after 30 minutes N_d^{exp} in the large apparatus has not reached the target value 2×10^8 particle/ml. The nanobubble number density per cell per cycle ρ_d^{exp} of small apparatus is 2.4 times larger than ρ_d^{exp} of large apparatus.

Table 8 shows the comparison of analysis results of large and small apparatus along Path3. It can be seen that the maximum shear stress $\tau_{max}^{pin=0.16} = 30\text{Pa}$ of small apparatus is about 1.3 times large than $\tau_{max}^{pin=0.45} = 24\text{Pa}$ of large apparatus, although the small apparatus has smaller average velocity and smaller pressure drop.

According to the experimental and analysis results, the nanobubble generation ability of the small apparatus is 2.4 times larger than that of the large apparatus, the maximum shear stress $\tau_{max}^{pin=0.16} = 30\text{Pa}$ of small apparatus is 1.3 times larger than

$\tau_{max}^{p_{in}=0.45}=24\text{Pa}$ of large apparatus. In this study, two kinds of honeycomb cells are compared. The small apparatus includes honeycomb cell width $w=3.9\text{mm}$ and honeycomb cell height $h=4\text{mm}$ and the large apparatus includes honeycomb cell width $w=6.1\text{mm}$ and honeycomb cell height $h=10\text{mm}$ as shown in Fig.3 and Table.7. From Table 8, with decreasing honeycomb dimension, τ_{max} may increase under the same inlet pressure p_{in} . Under the same $p_{in}=0.45\text{MPa}$, the maximum shear stress $\tau_{max}^{p_{in}=0.45}=56\text{Pa}$ of small apparatus is 2.3 times larger than $\tau_{max}^{p_{in}=0.45}=24\text{Pa}$ of large apparatus. These results show that the shear stress τ_{max} may control the nanobubble generation ability.

Table 7. Comparison of nanobubble generation ability

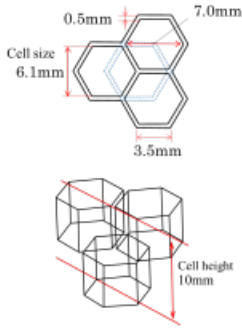
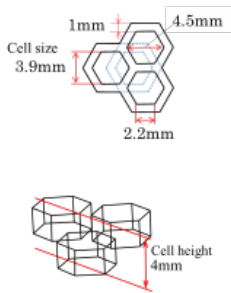
	Item		Large model	Small model
Experimental condition	Output	$P_w[\text{kW}]$	3.7[kW] (60Hz)	0.4[kW] (60Hz)
	Number of cells	N_{cell}	3510	1840
	Flow rate	$Q[\text{l}/\text{min}]$	550[l/min]	103[l/min]
	Water amount	$V[\text{l}]$	1000[l]	100[l]
	Experiment time	$t[\text{min}]$	30[min]	30[min]
	Number of cycle	N_{cycle}	33	31
Experimental results	Nanobubble number density after 30min	N_d^{exp} [particle/ml]	$N_d^{exp} = 1.7 \times 10^8$ [particle/ml]	$N_d^{exp} = 4.3 \times 10^8$ [particle/ml]
	Nanobubble number density per cell per cycle	ρ_d^{exp} [particle/ml]	$\rho_d^{exp} = 3.13 \times 10^3$ [particle/ml]	$\rho_d^{exp} = 7.61 \times 10^3$ [particle/ml]
Cell dimensions	Honeycomb cell width	$w[\text{mm}]$,	6.1 [mm]	3.9 [mm]
	Honeycomb cell height	$h[\text{mm}]$	10 [mm]	4 [mm]
				

Table 8. Comparison of analysis results at Path3

Analysis condition	Item		Large apparatus	Small apparatus	
	Inlet absolute pressure	p_{in} [MPa]	Experimental pressure	Experimental pressure	Equal pressure
			0.45[MPa]	0.16[MPa]	0.45[MPa]
Analysis results	Average velocity	v [m/s]	$v^{p_{in}=0.45} = 0.71$ [m/s]	$v^{p_{in}=0.16} = 0.40$ [m/s]	$v^{p_{in}=0.45} = 0.95$ [m/s]
	pressure drop	Δp [MPa]	$\Delta p^{p_{in}=0.45} = 0.03$ [MPa]	$\Delta p^{p_{in}=0.16} = 0.01$ [MPa]	$\Delta p^{p_{in}=0.45} = 0.07$ [MPa]
	Shear stress	τ_{max} [Pa]	$\tau_{max}^{p_{in}=0.45} = 24$ [Pa]	$\tau_{max}^{p_{in}=0.16} = 30$ [Pa]	$\tau_{max}^{p_{in}=0.45} = 56$ [Pa]

5. Results of CFD-PBM analysis

5.1 Bubble size distribution in small apparatus

The bubble size distribution in a small apparatus is simulated using CFD-PBM method. Table 5 shows the inlet boundary condition, pressure boundary condition 0.16MPa. As the outlet boundary condition, pressure boundary condition 0.10MPa is adopted, which is the same as atmospheric pressure. The gas volume fraction is 0.00971 at the inlet. The bin 8 specifying 1280nm is chosen as the initial bubble size at the inlet.

Figure 6 shows the nanobubble number density $N_d(x)$ in the tank, which is obtained from the CFD-PBM simulation results at the outlet $N_d^{pbm}(x)$. The simulation result $N_d(x)$ in the tank is obtained from

$$N_d(x) = \frac{N_d^{pbm}(x) \cdot Q \cdot t}{V_{tank}} \quad (14)$$

where Q is the flow rate, Q=103L/min, t is the experiment time, t=30min, and V_{tank} is the volume of water in the tank, $V_{tank}=100\text{l}$. Notation $N_d(x)$ denotes the number density of the bubbles generated from the apparatus. The original bubbles or other particles $N_d^{exp}(x)|_{t=0}$ in the water tank when t=0min are not included. The 30-minute experimental result $N_d^{exp}(x)|_{t=30}$ includes the origin bubbles or other particles.

Nano Sight LM10-HS used in this study can detect the bubbles with the diameter in the range $x = 0 - 1000\text{nm}$. As shown in Table 6, the bubble bin number 1 – 7 are set with in this diameter range. This is to focus on the small bubbles and to be compared with the experimental results $N_d^{exp}(x)$. Fig.6 shows that the difference is about 13% between the PBM and experimental results at 70nm diameter. Therefore, it is seen that the simulation can predict sufficiently.

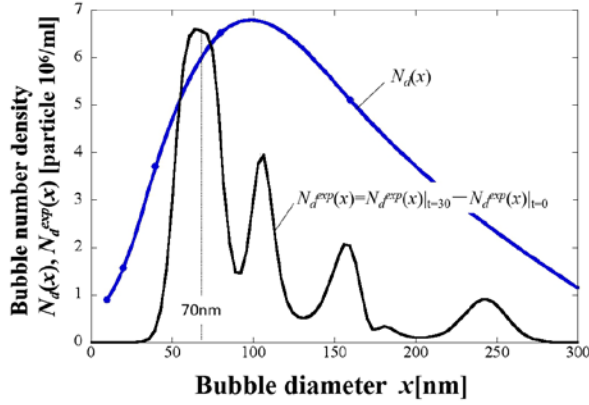


Figure 6. Bubble number density $N_d(x)$, $N_d^{exp}(x)$ of small apparatus in the tank

5.2 The maximum shear stress and nanobubble number density distribution under different inlet absolute pressure

Fig.7 shows the nanobubble number density $N_d(x)$ by varying inlet absolute pressure. With increasing the inlet absolute pressure, the number nanobubble density increases continuously, and the most predominant bubble size becomes larger. From the experimental results of the small apparatus, the number of bubbles diameters 70nm is predominant. Therefore, in the following discussion, the number density of bubbles with 70nm in diameter $N_d(70)$ is focused.

Fig.8 shows the CFD analysis results for maximum shear stress at Path3 by varying inlet absolute pressure of the small apparatus. With increasing the inlet absolute pressure, the maximum shear stress increases and finally saturated around $p_{in}=0.5$ MPa.

The nanobubble number density distributions are analyzed by using the CFD-PBM by varying the inlet absolute pressure from $p_{in}=0.16$ MPa to $p_{in}=0.6$ MPa. Table 9 shows the analysis conditions under the inlet gas flow rate is fixed as $1\ell/\text{min}$.

Table 9. PBM analysis conditions for varying p_{in} under fixed inlet gas flow rate $1\ell/\text{min}$

Inlet absolute pressure p_{in} [MPa]	Outlet absolute pressure [MPa]	Gas fraction	volume	Initial bubble size [nm]
0.16	0.1	0.00971		1280
0.2	0.1	0.00769		1280
0.25	0.1	0.00639		1280
0.3	0.1	0.0056		1280
0.4	0.1	0.00463		1280
0.45	0.1	0.00451		1280
0.5	0.1	0.00405		1280
0.6	0.1	0.00363		1280

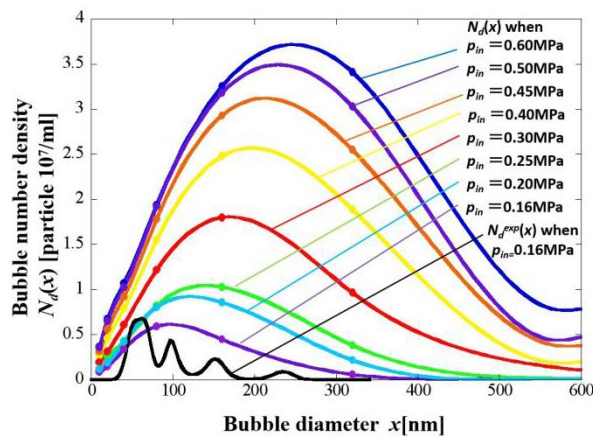


Figure 7. Bubble number density $N_d(x)$ by varying inlet absolute pressure p_{in} .

Fig. 8 shows the variation of maximum shear stress and nanobubble density $N_d(70)$ by varying inlet absolute pressure p_{in} . With increasing the inlet absolute pressure p_{in} , the maximum shear stress increases and saturates at $p_{in}=0.4$ MPa. The density $N_d(70)$ also increases with increasing p_{in} and finally saturates at $p_{in}=0.5$ MPa. Fig. 9 shows the maximum shear stress and the nanobubble density $N_d(70)$. With increasing maximum shear stress, $N_d(70)$ also increases. It may be concluded that the maximum shear stress is the main controlling factor for the nanobubble generation.

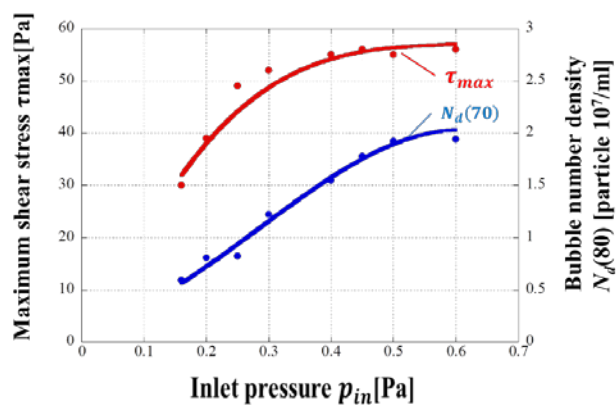


Figure 8. Maximum shear stress τ_{max} and bubble number density $N_d(70)$ by varying inlet absolute pressure p_{in} .

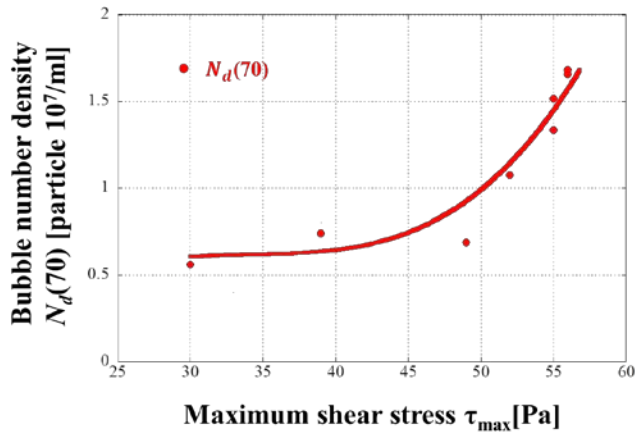


Figure 9. Bubble number density $N_d(70)$ vs maximum shear stress τ_{max}

6. Conclusions

Several previous studies discussed in generation of microbubble whose diameter is 1- 100 μm . However, no detail study is available for nanobubble whose diameter is less than 0.1 μm . Therefore, in this paper, nanobubble generation mechanism and generation ability will be studied for the small apparatus as well as large apparatus using different honeycomb structures based on the results of experiment and CFD-PBM analysis.

- (1) The maximum shear stress τ_{max} appears at the vicinity of the honeycomb cell corner. The maximum shear stress τ_{max} of small apparatus is larger than τ_{max} of large apparatus.
- (2) The experiment and the PBM analysis show that the nanobubble number density N_d in honeycomb cell of small apparatus is also larger than N_d of large apparatus.
- (3) The maximum shear stress is the main controlling factor for the nanobubble generation since the nanobubble number density N_d increases with increasing the maximum shear stress τ_{max} .

Acknowledgement

This research was supported by Ministry of Economy, Trade and Industry, METI Strategic Foundational Technology Improvement Support Operation (Heisei 26, 20140910). The authors wish to express our thanks to our group member Mr. Takahiko Ueda for his generous support to this project.

Symbols used

$B_{ag,i}$	[-]	birth rate of bubbles due to aggregation
$B_{br,i}$	[-]	birth rate of bubbles due to breakage
$D_{ag,i}$	[-]	death rate of bubbles due to aggregation
$D_{br,i}$	[-]	death rate of bubbles due to breakage
e_{ij}	[-]	strain tensor
$g(V')$	[-]	Rate of bubbles with volume V' splitting per unit time
h	[mm]	honeycomb cell height
i	[m]	bubble size
I	[-]	shear strain rate
K	[-]	turbulent kinetic energy [m^2/s^2]
N_i	[-]	volume with bubble size i
N_{cell}	[-]	number of cells
N_{cycle}	[-]	number of cycle
N_d^{exp}	[particle/ml]	experimental nanobubble number density
$N_d^{pbm}(x)$	[particle/ml]	nanobubble number density obtained by PBM analysis
p_a	[MPa]	absolute pressure
p_{in}	[MPa]	inlet pressure
P_w	[kw]	power
Q	[l/min]	flow rate
t	[s]	experiment time
T_I	[%]	Turbulent intensity
U_{ave}	[m/s]	Average velocity
U_i	[m/s]	velocity components
V_i	[m^3]	volume of the bubble size
V, V'	[m^3]	volume before change, volume after change
V_{tank}	[m^3]	tank capacity
w	[mm]	honeycomb cell width
z/h	[-]	dimensionless coordinate
α_i	[m^3]	volume fraction
$\beta(V/V')$	[-]	Probability density function bursting from volume V
Δp	[MPa]	pressure drop
E	[-]	turbulent dissipation rate [m^2/s^3]
λ	[-]	The number of burst bubbles generated per pre-split bubble
ρ_q	[kg/m^3]	density of the q^{th} phase
ρ_d^{exp}	[$1/m^3$]	nanobubble number density per cell per cycle
τ	[Pa]	shear stress
τ_{max}^{pin}	[Pa]	maximum shear stress
Ω_{ag}	[$1/m^3s$]	aggregation kernel
Ω_{br}	[$1/m^3s$]	breakage kernel

References

- [1] K. Fukushi, Y. Matsui, N. Tambo, *J. Water SRT-Aqua*, **1998**, 47, 76-86. DOI:[10.2166/aqua.1998.13](https://doi.org/10.2166/aqua.1998.13)
- [2] H. Onari, T. Saga, K. Watanabe, K. Maeda, K. Matsuo, *The Resources Processing Society of Japan*, **1999**, 46, 238-244. DOI:[10.4144/rpsj1986.46.238](https://doi.org/10.4144/rpsj1986.46.238)
- [3] I. Kakuta, *Bull. Soc. Sea Water Sci., Jpn*, **2006**, 60,160-163. DOI:[10.11457/swsj1965.60.160](https://doi.org/10.11457/swsj1965.60.160)
- [4] H. Tsuge, *Bull. Soc. Sea Water Sci., Jpn*, **2010**, 64, 4-10. DOI:[10.11457/swsj.64.4](https://doi.org/10.11457/swsj.64.4)
- [5] M. Takahashi, *Materials integration*, **2009**, 22, 2-19.
- [6] K. Michioku, T. Kanda, H. Ohnari, T. Nishikawa, K. Matsuo, T. Kido, *Proc. 44th Int. Hydraulics Engineering Japan Society of Civil Engineers*, Tokyo, **2000**, 1119-1118. DOI:[10.2208/prohe.44.1119](https://doi.org/10.2208/prohe.44.1119)
- [7] H. Hasegawa, Y. Masaki, K. Matsuuchi, Y. Yoshida, *Trans. JSME*, **2006**, 72, 160-166. DOI: [10.1299/kikaib.72.2242](https://doi.org/10.1299/kikaib.72.2242)
- [8] S. Ueyama, M. Miyamoto, *The World of Micro Bubbles*, Kogyo Chosakai Publishing, **2006**, 1-203.
- [9] T. Makuta, *Acoustical Society of Japan*, **2017**, 6, 417-423. DOI:[10.20697/iasj.73.7_417](https://doi.org/10.20697/iasj.73.7_417)
- [10] K. Mituda, *The Surface Finishing of Japan*, **2017**, 7, 331-334. DOI:[10.4139/sfj.68.331](https://doi.org/10.4139/sfj.68.331)
- [11] K. Hiraki, *The Latest Technology on Microbubbles and Nanobubbles*, CMC Publishing, Tokyo, **2014**, 2,177-183.
- [12] M. Sadatomi, A. Kawahara, K. Kano, A. Ohtomo, *Experimental Thermal and Fluid Science*, **2005**, 29, 615-623. DOI: [10.1016/j.exptthermflusci.2004.08.006](https://doi.org/10.1016/j.exptthermflusci.2004.08.006)
- [13] H. Tsugei, *The Latest Technology on Microbubbles and Nanobubbles II*, CMC Publishing, Tokyo, **2010**, 6-10.
- [14] H. Tsuji, *Proc. 3th Int. The Japanese Society for Multiphase Flow*, Osaka, **2009**, 214-215.
- [15] Y. Yonezawa et al, *Regional Innovation Creation Research and Development Project Outcome Report "Development of a Honeycomb Type Mixer for Uniformization of Nanobubbles and Its Application to Industry"*, **2012**, Kyushu Bureau of Economy, Trade and Industry and Kyushu Industrial Technology Center, 2-31.
- [16] Y. Kudo, K. Hiraki, *Proc. 3th Int. The Japan Society for Design Engineering Micro-Nano Science & Technology division*, Tokyo, **2011**, 26-27. DOI:[10.1299/jsmemnm.2011.3.129](https://doi.org/10.1299/jsmemnm.2011.3.129)
- [17] Y. Kudo, K. Hiraki, *Proc. National conference of JSME Micro-Nano Science & Technology Division*, Tokyo, **2010**, 2, 95-96.
- [18] N.-A. Noda, F. Ren, W. Yamamoto, T. Ueda, Y. Sano, D. Chen, Y. Takase, Y. Yonezawa, *Japan Society for Design Engineering*. **2018**, 53, 111–126. DOI:[10.14953/ijsde.2016.2707](https://doi.org/10.14953/ijsde.2016.2707)
- [19] F. Ren, N.-A. Noda, T. Ueda, Y. Sano, Y. Takase, T. Umekage, Y. Yonezawa and H. Tanaka, *Journal of Dispersion Science and Technology*, **2018**, 40(2), 306-317. DOI:[10.1080/01932691.2018.1470009](https://doi.org/10.1080/01932691.2018.1470009)

- [20] T.-F. Wang, J.-F. Wang, Y. Jin, *Ind. Eng. Chem. Res.*, **2005**, 44, 7540-7549.
DOI:[10.1021/ie0489002](https://doi.org/10.1021/ie0489002)
- [21] L.-M. Li, Z.-Q. Liu, B.-K. Li, H. Matsuura, F. Tsukihashi, *ISIJ International*, **2015**, 55, 1337-1346. DOI:[10.2355/isijinternational.55.1337](https://doi.org/10.2355/isijinternational.55.1337); A. Malloy, B. Car: Particle & Particle Systems Characterization, **2006**, 23, 197-204.
- [22] V. Filipe, A. Hawe, W. Jiskoot: *Pharmaceutical Research*, **2010**, 27, 796-810.
- [23] A. Malloy, B. Car, *Particle & Particle Systems Characterization*, **2006**, 23, 197-204.
- [24] ANSYS®, *Academic Research*, Release16.2, ANSYS Inc.
- [25] R. Sano, *Continuum Dynamics*, Asakura Publishing, Tokyo, **2007**, 46.
- [26] T. Wang, J. Wang, *Chem. Eng. Sci.*, **2007**, 62, 7107-7118.
DOI:[10.1016/j.ces.2007.08.033](https://doi.org/10.1016/j.ces.2007.08.033)
- [27] T. Wang, J. Wang, Y. Jin, *AIChE Journal*, **2006**, 52, 125-140.
DOI:10.1002/aic.10611
- [28] D. Drew, *Annual Review of Fluid Mechanics*, **1983**, 15, 261-291
DOI:10.1146/annurev.fl.15.010183.001401
- [29] R. Krishna, M.-I. Urseanu, J.-M. Van Baten, J. Ellenberger, *Chem. Eng. Sci.*, **1999**, 54, 4903-4911. DOI:[10.1016/S0009-2509\(99\)00211-0](https://doi.org/10.1016/S0009-2509(99)00211-0)
- [30] L. Hagesaether, H.-A. Jakobsen, H.-F. Svendsen, *Chem. Eng. Sci.*, **2002**, 57, 3251-3267. DOI:[10.1016/S0009-2509\(02\)00197-5](https://doi.org/10.1016/S0009-2509(02)00197-5)

Table and Figure captions

Table 1. Comparison of nanobubble generation ability

Table 2. Details of the experimental apparatus

Table 3. Experimental conditions between the large and small apparatus

Table 4. Analysis conditions for small apparatus

Table 5. CFD-PBM analysis conditions of the small apparatus

Table 6. Diameter of each bubble bin

Table 7. Comparison of nanobubble generation ability

Table 8. Comparison of analysis results at Path3

Table 9. PBM analysis conditions for varying p_{in} under fixed inlet gas flow rate
1ℓ/min

Figure 1. (a) Large and (b) Small apparatus including parallel honeycomb unit, and (c) Illustration of a honeycomb unit.

Figure 2. Nanobubbles number density variation for large and small apparatus after the experiment starts

Figure 3. Periodic 3-row model used for large and small apparatus

Figure 4. (a) Shear stress variation with the definition of Path1- 6, (b) Shear stress distribution along the path for fixed distance d from the wall.

Figure 5. Absolute pressure and shear stress distribution and path (a)(b)(c) is longitudinal, path (d)(e)(f) is lateral in **Fig.4**

Figure 6. Bubble number density $N_d(x), N_d^{exp}(x)$ of small apparatus in the tank

Figure 7. Bubble number density $N_d(x)$ by varying inlet absolute pressure p_{in} .

Figure 8. Maximum shear stress τ_{max} and bubble number density $N_d(70)$ by varying inlet absolute pressure p_{in} .

Figure 9. Bubble number density $N_d(70)$ vs maximum shear stress τ_{max}

Graphical Abstracts

The maximum shear stress τ_{max} appearing repeatedly around honeycomb cell corners controls the nanobubble generation. The experiment and CFD-PBM results show bubble number density with 70nm in diameter $N_d(70)$ increases with increasing the maximum shear stress τ_{max} .

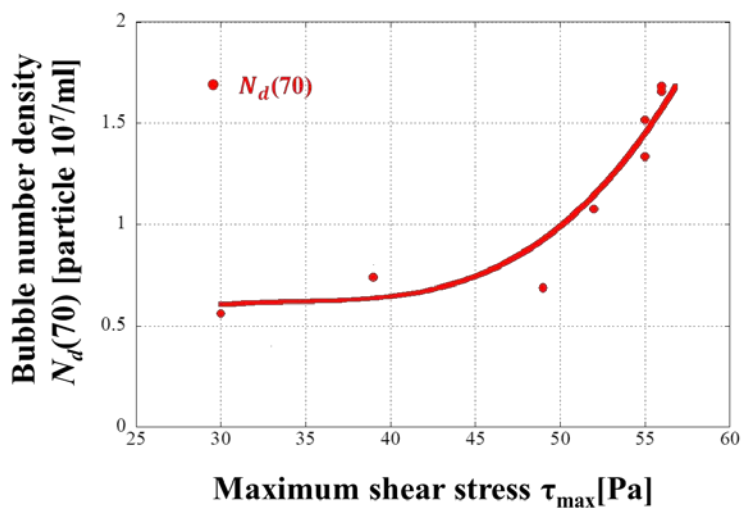


Figure. Bubble number density with 70nm in diameter $N_d(70)$ vs maximum shear stress τ_{max}